# Intracellular determinants of CA1 pyramidal cells activation or silencing during locomotion Authors

François-Xavier Michon, Geoffrey Marti, Caroline Filippi, Romain Bourboulou, Julie Koenig, Jérôme Epsztein

## Title

# Intracellular determinants of CA1 pyramidal cells activation or silencing during locomotion


## Authors

François-Xavier Michon[1], Geoffrey Marti[1], Caroline Filippi[1], Romain Bourboulou[1], Julie Koenig[1] and Jérôme Epsztein[1]*

## Authors Affiliation:

(1) National Institute for Health and Medical Research (INSERM UMR 1249), Aix-Marseille University, Institute of Neuroscience of the Mediterranean Sea (INMED)

## * Corresponding Author:

Jérôme Epsztein

jerome.epsztein@inserm.fr

Phone : ±33 0 4 91 82 81 47

INMED/INSERM U1249

Parc Scientifique de Luminy

163 route de Luminy

13273 Marseille Cedex 09

# Abstract

Spontaneous locomotion strongly influences the state of the hippocampal network and is critically important for spatial information coding. However, the intracellular determinants of CA1 pyramidal cells activation during locomotion are poorly understood. Here we recorded the membrane potential of CA1 pyramidal cells (PCs) while non-overtrained mice spontaneously alternated between periods of movement and immobility during a virtual spatial navigation task. We found opposite membrane polarization between bursting and regular firing CA1 PCs during movement. Regular firing CA1 PCs were more depolarized and fired at higher frequency during movement compared to immobility while bursting CA1 PCs, located deep in the CA1 pyramidal cell layer and preferentially inhibited during sharp wave ripples, were hyperpolarized during movement in a speed dependent manner. This speed-dependent suppression of a subpopulation of CA1 PCs could enhance signal to noise ratio for efficient spatial coding during locomotion.



# Keywords

Hippocampus; place cells; CA1 pyramidal cells; locomotion; patch-clamp; in vivo

# Introduction

Spontaneous locomotion strongly modulates sensory perception and learning. In the neocortex, active exploration notably through locomotion can modify the response of neurons to sensory stimuli, and associated task performance (Crochet and Petersen, 2006; Niell and Stryker, 2010; Polack et al., 2013; McGinley et al., 2015; Vinck et al., 2015; Albergaria et al., 2018). Locomotion also profoundly modify hippocampal network dynamics and coding (Vanderwolf, 1969). During movement, the hippocampal local field potential (LFP) is dominated by theta (7-12 Hz) oscillations and activated hippocampal cells show place specific activity (O'Keefe and Dostrovsky, 1971; McNaughton et al., 1983; Wilson and McNaughton, 1993; Moser et al., 2017). This state is often referred to as the "online" state of the hippocampus when coding of spatial, temporal or contextual information occurs. During immobility, the hippocampal LFP is interrupted by large negative transients, called sharp waves during which fast oscillations or ripples (O'Keefe and Nadel, 1978; Buzsáki et al., 1992) organize the firing of hippocampal cells into sequences representing past or future locations (Buzsaki, 1989; Foster and Wilson, 2006; Gupta et al., 2010; Pfeiffer and Foster, 2013; Buzsáki, 2015).

The cellular mechanisms of hippocampal pyramidal cells' activation during locomotion are poorly understood. Active exploration is often associated with membrane potential depolarization of pyramidal cells in the somatosensory and visual cortex (Crochet and Petersen, 2006; Bennett et al., 2013; Arroyo et al., 2018), which could constitute a permissive state for sparse sensory coding. In the hippocampus, pyramidal cells active during locomotion (the place cells) show a systematic bump of depolarization in specific places leading to place-specific firing (the place field) but remains relatively hyperpolarized outside the place field (Harvey et al., 2009; Epsztein et al., 2011; Bittner et al., 2015; Cohen et al.,

2017; Grienberger et al., 2017) while silent cells have a uniform baseline $V_m$ far away from threshold in every part of the environment (Epsztein et al., 2011; Bittner et al., 2015). However, the baseline $V_m$ values of place and silent cells during locomotion largely overlap, ruling out a simple depolarized permissive state as the main difference explaining their activation. Alternatively, it could result from differences in their intrinsic membrane properties. Place cells in a new environment have a high intrinsic frequency of action potential firing (burst firing cells) even before the start of exploration while silent cells fire more regularly (regular firing cells) (Epsztein et al., 2011). Furthermore, depolarizing a silent cell by a constant current injection during locomotion is sufficient to induce place cell coding (Lee et al., 2012). Burst and regular firing cells could also correspond to two different cell types (Kandel and Spencer, 1961; Graves et al., 2012) that are differently engaged during locomotion. Finally, hippocampal cells silent during locomotion could be selectively suppressed through dedicated inhibitory sub circuits (Lapray et al., 2012; Arriaga and Han, 2017).

To decipher between these scenarios, we combined whole-cell patch-clamp recordings of hippocampal CA1 pyramidal cells with extracellular field recordings using a multi-site linear silicon probe while head-fixed mice alternated spontaneously between periods of locomotion and immobility during a spatial navigation task in a familiar virtual reality environment. Intracellular recordings allowed us to probe CA1 pyramidal cells' intrinsic properties through direct current injections and the effect of locomotion on their $V_m$ dynamics. We describe an opposite membrane potential polarization of bursting and regular firing CA1 pyramidal cells during locomotion.

# Results

## Whole-cell membrane potential recordings during spatial navigation in virtual reality

Whole-cell current-clamp recordings were obtained from CA1 pyramidal cells in the dorsal hippocampus of head-restrained mice running on a circular treadmill (Fig. S1A) as they explored a linear virtual maze (Fig. S1B) enriched with different patterns and virtual 3D objects for water rewards (Fig. S1C). Because mice were not over trained (1.15 ± 0.26 reward/min; n = 17 recording sessions) they spontaneously alternated periods of immobility and movement during exploration (ratio time in immobility vs time in movement = 0.48 ± 0.04; n = 17 recording sessions). This spontaneous behavior allowed us to analyze CA1 pyramidal cells' membrane potential ($V_m$) and firing during immobility and movement periods. In a subset of recordings LFP activity was recorded simultaneously to assess $V_m$ behavior during ripples spontaneously occurring during immobility periods.

## Heterogeneous membrane potential dynamics of CA1 PCs during movement

We analyzed data from 17 whole-cell recordings of CA1 pyramidal cells in 14 mice. To assess CA1 pyramidal cell $V_m$ modulation during transitions from immobility to movement we calculated a modulation index (see methods). The vast majority of CA1 pyramidal cells (n = 16 out of 17; 94%) were significantly modulated during switches in behavioral states. Among those cells, a majority (n = 10 out of 16; 62.5%) was negatively modulated meaning that their membrane potential was significantly more hyperpolarized during movement compared to immobility (HypM cells). A trace from a representative HypM CA1 pyramidal cell is illustrated in Fig. 1A. The membrane potential was consistently more hyperpolarized (Fig. 1A, B) and firing rate lower (Fig. 1A, C) during periods of movement. We note that this $V_m$ behavior is

opposite to what is observed in layer 2/3 cortical pyramidal cells during movement (Polack et al., 2013). On the other hand, $V_m$ variance was consistently lower (Fig. 1A, D) during movement, which is consistent with cortical pyramidal cells. This decrease was more pronounced for low frequency oscillations (Fig. 1E). To get an idea of the kinetics of these changes we focused on the times of transitions between immobility and movement periods and vice versa. The kinetics of $V_m$ changes (Fig. 1F, middle) mimicked the kinetics of behavioral changes (Fig. 1F, top), which were faster for immobility to movement transitions. The effect was consistent from transition to transition in both directions (Fig. 1F, bottom). The other type of modulated cells (n = 6 out of 16; 37.5%) was positively modulated meaning that their membrane potential was significantly more depolarized during movement (DepM cells). A trace from a representative DepM cell is represented in Fig. 2A. For this cell, the membrane potential was consistently more depolarized during movement versus immobility periods (Fig. 2A, B) and the firing rate was higher (Fig. 2A, C). Note that in this cell most action potentials were driven by underlying spikelets (Epsztein et al., 2010; Fig. 2A, inset). When focusing on the transition periods (Fig. 2F) we also observed a fast depolarization (hyperpolarization) upon transition to movement (immobility) but with a small time-lag compared to HypM cells. The transition by transition visualization (Fig. 2F, bottom) also revealed the consistency of the modulation.

On average, HypM CA1 pyramidal cells displayed a ~2 mV hyperpolarization during movement (Mov: - 60.5 ± 3.02 mV; Imm: -58.4 ± 3.13 mV; n = 10 cells, $P < 10^{-3}$, paired *t*-test; Fig. 3A), reduced variability (Mov: 4.26 ± 1.01 $mV^2$; Imm: 6.44 ± 1.20 $mV^2$; n = 10 cells, $P$ = 0.015, paired *t*-test; Fig. 3C) and reduced firing rate (Mov: 3.06 ± 1.80 Hz; Imm: 6.37 ± 1.88 mV; n = 8 cells, $P = 6 \times 10^{-3}$, paired *t*-test; Fig. 3B). The same conclusions were reached when analyzing all the transitions for HypM cells independently (Fig. S2; $V_m$ expressed as Z-score).

For immobility to movement transitions (Fig. S2A-C, top), the $V_m$ was hyperpolarized (Mov: -0.5 ± 0.06; Imm: 0.17 ± 0.06; n = 127 transitions, $P < 10^{-13}$, paired *t*-test), firing rate was decreased (Mov: 2.04 ± 0.53 Hz; Imm: 3.35 ± 0.48 Hz; n = 127 transitions with firing, $P < 10^{-6}$, signed rank test) and variance was decreased (Mov: 2.24 ± 0.21 $mV^2$; Imm: 3.87 ± 0.26 $mV^2$; n = 127 transitions, $P < 10^{-8}$, signed rank test).

In DepM CA1 pyramidal cells, the depolarization during movement was smaller ~0.6 mV (Mov: -62.4 ± 3.57 mV; Imm: -63.0 ± 3.61 mV; n = 6 cells, $P = 0.006$, paired *t*-test; Fig. 3A) and the $V_m$ variance was not significantly different (Mov: 3.35 ± 0.81 $mV^2$; Imm: 2.52 ± 0.71 $mV^2$; n = 6 cells, $P = 0.17$, paired *t*-test; Fig. 3C). Accordingly, the firing rate was not significantly modulated for these cells (Mov: 2.73 ± 1.49 Hz; Imm: 2.04 ± 1.3 $mV^2$; n = 4 cells, $P = 0.13$, paired *t*-test; Fig. 3B). When analyzing all transitions from immobility to movement (Fig. S2A-C, bottom), qualitatively similar results were observed: a small depolarization (Mov: 0.12 ± 0.04; Imm: - 0.26 ± 0.04 mV; n = 180 transitions, $P < 10^{-12}$, paired *t*-test) without significant change in the variance (Mov: 2.01 ± 0.13 $mV^2$; Imm: 2.04 ± 0.12 $mV^2$; n = 180 transitions, $P < 10^{-12}$, signed rank test) yielding a small but significant increase in firing rate (Mov: 1.98 ± 0.28 Hz; Imm: 1.38 ± 0.18 Hz; n = 180 transitions, $P = 10^{-4}$, signed rank test).

We note that HypM cells were on average more depolarized than DepM cells during immobility (HypM: -58.4 ± 3.13 mV, n = 10 cells; DepM: -63.0 ± 3.61 mV, n = 6 cells; $P = 0.37$,unpaired *t*-test). To determine if this difference could account for the opposite modulation between HypM and DepM cells by locomotion we excluded all HypM cells more depolarized than -55 mV during immobility. This strongly reduced the difference in baseline $V_m$ between HypM and DepM cells (HypM: -64.6 ± 2.76 mV, n = 6 cells; DepM: -63 ± 3.61 mV,

n = 6 cells; *P* = 0.73, unpaired *t*-test). However, HypM cells were still on average hyperpolarized by ~1.7 mV during movement (Mov: - 66.3 ± 2.76 mV; Imm: -64.6 ± 2.76 mV; n = 6 cells, *P* = 0.038, paired *t*-test). Thus, although we cannot exclude a contribution of baseline $V_m$ differences between HypM and DepM cells in the effect we observed, the effect can still be observed when this difference is strongly reduced. The difference between HypM and DepM cells was also not related to changes in animal performance in terms of number of reward per minute (HypM: 1.08 ± 0.44, n = 10 recording sessions; DepM: 1.2 ± 0.23, n = 6 recording sessions; *P* = 0.18, rank sum test; Fig. S3) or ratio of time spent in movement and immobility (HypM: 0.44 ± 0.06, n = 10 recording sessions; DepM: 0.55 ± 0.04, n = 6 recording sessions; *P* = 0.25, rank sum test; Fig. S2).

**Heterogeneous speed dependent modulation of membrane potential dynamics in CA1 PCs**

Previous extracellular recordings report a speed dependent modulation of CA1 pyramidal cells firing rate during locomotion (McNaughton et al., 1983; Czurkó et al., 1999). We wondered whether similar speed dependent modulation could be observed at the subthreshold level. For each HypM and DepM cells we calculated the correlation between the Z-scored $V_m$ and speed binned at 0.05 $cm.s^{-1}$. A majority of HypM (n = 8 out of 10) showed significant and negative correlations between speed and $V_m$. Two example cells are shown in Fig. 4A (top) for recordings performed in a slow (maximal running speed ~6 $cm.s^{-1}$) and a fast (maximal running speed ~15 $cm.s^{-1}$) animal. In both cases the faster the animal ran the more the cell got hyperpolarized. As a population, HypM cells were significantly and negatively modulated by speed (r: - 0.46 ± 0.09; n = 10, *P* < 0.001, one sample *t*-test; Fig. 4B). Only half of DepM cells showed significant and positive correlation between speed and $V_m$.

Two example cells are shown in Fig. 4 A (bottom) for recordings performed in a slow (maximal running speed ~8 $cm.s^{-1}$) and a fast (maximal running speed ~15 $cm.s^{-1}$) animal. As a population, DepM cells showed no significant correlation between $V_m$ and speed (r: 0.27 ± 0.14; n = 6, $P = 0.1$, one sample *t*-test).

**Opposite membrane potential modulation of bursting and regular firing CA1 PCs during movement**

Our initial analysis revealed that CA1 pyramidal cells can be divided into two subgroups based on their membrane potential and firing rate modulations during locomotion. A first group (HypM cells) showed a large and speed dependent hyperpolarization together with reduced variance and firing rate during locomotion while a second group showed more moderate depolarization without significant change in variance and a smaller increase in firing rate. Previous *in vivo* whole-cell recordings in freely moving rats exploring a new environment have revealed differences in CA1 pyramidal cell activation during locomotion between bursting and regular firing cells (Epsztein et al., 2011). We next thought to determine if different intrinsic properties could also exist between HypM and DepM CA1 pyramidal cells in head-fixed mice exploring a familiar environment. We thus analyzed the response of HypM and DepM cells to depolarizing pulses of current injected *via* the patch pipette before exploration of the virtual environment. As in anesthetized rats, distinct bursting and regular firing behaviors could be observed among CA1 pyramidal cells recorded in awake mice (Fig. 5A). Unexpectedly, HypM cells exhibited far more bursting than DepM cells (fraction of APs in burst or bursting index, HypM: 0.79 ± 0.08, n = 10; DepM: 0.21 ± 0.11, n = 6, $P < 10^{-3}$, unpaired *t*-test; Fig. 5B). Over all recorded cells there was a significant

correlation between bursting and modulation indexes (r = - 0.66; *P* = 0.003; Fig. 5C). Other pre-exploration intrinsic parameters were not significantly different between HypM and DepM cells. This was the case for pre-exploration baseline membrane potential (HypM: -65.1 ± 2.15, n = 10; DepM: - 68.5 ± 3.47; n = 6, *P* = 0.39,unpaired *t*-test; Fig. 5D), the firing threshold (HypM: -52.0 ± 2.02, n = 10; DepM: - 51.8 ± 3.42, n = 6; *P* = 0.36,unpaired *t*-test; Fig. 5E), the difference between firing threshold and baseline $V_m$ (HypM: 13.1 ± 1.32, n = 10; DepM: 16.75 ± 4.39, n = 6; *P* = 0.36, ranksum *t*-test; Fig. 5F), the input resistance (HypM: 44.9 ± 5.06, n = 10; DepM: 43.3 ± 3.39, n = 6; *P* = 0.83, unpaired *t*-test; Fig. 5G) and the rheobase ( HypM: 116 ± 87, n = 10; DepM: 294 ± 107, n = 6; *P* = 0.24, unpaired *t*-test; Fig. 5H).

**Heterogeneous membrane potential modulation of CA1 PCs during sharp-wave ripples**

Sharp waves ripple (SWRs) are transient events recorded in the local field potential of CA1 during periods of immobility, slow wave sleep and anesthesia (Girardeau and Zugaro, 2011; English et al., 2014; Buzsáki, 2015; Roumis and Frank, 2015; Valero et al., 2015; Colgin, 2016; Hulse et al., 2016; Gan et al., 2017). They result from the dendritic excitation of CA1 pyramidal cells dendrites by the synchronous discharge of upstream CA3 pyramidal neurons. Recently, different anatomically defined CA1 pyramidal cells were shown to be differently modulated during SWRs (Valero et al., 2015) with CA1 pyramidal cells located deep in the pyramidal cell layer (close to stratum oriens) preferentially hyperpolarized and cells located more superficially in the pyramidal cell layer (closer to stratum radiatum) preferentially depolarized. To see if similar differential modulation could be observed between HypM and DepM CA1 pyramidal cells, we analyzed intracellular $V_m$ modulations during ripples recorded

in the LFP using a linear silicon probe. A majority of HypM cells (n = 5/8; 62.5%) were preferentially hyperpolarized during ripples with other HypM cells not significantly modulated while DepM cells showed a mixed behavior. Overall, HypM and Dep M cells were differently modulated during ripples (HypM: -2.35 ± 0.88, n = 8; DepM: 0.45 ± 0.84 mV, n = 6; $P$ = 0.046, unpaired $t$-test; Fig. 6A-C). This difference could not be explained by differences in pre-ripple baseline $V_m$ (HypM: -59.1 ± 3.36 mV, n = 8; DepM: -62.5 ± 3.78 mV, n = 6; $P$ = 0.52, unpaired $t$-test; Fig. 6D). To see if the preferential hyperpolarization of HypM cells could be correlated to the position of their cell body in the CA1 pyramidal cell layer we used post-hoc revelation of biocytin filled neurons. A staining against calbindin was used to mark more superficially located CA1 pyramidal cells and determine the border between stratum pyramidale and stratum radiatum (Valero et al., 2015). The cell bodies of the 6 HypM CA1 pyramidal cells successfully labeled were all 20 µm deeper that the border (mean: 39.2 ± 6.26 µm, n = 6; range: 23.7 – 68.2 µm) indicating that they were preferentially located deep within the CA1 pyramidal cell layer (Valero et al., 2015).

# Discussion

Locomotion is a strong modulator of hippocampal network dynamics (Vanderwolf, 1969) and is important for the sparse coding of spatial information by hippocampal place cells (Rowland et al., 2011). To get a better understanding of the cellular mechanisms of hippocampal cells activation (or silence) during locomotion, we recorded the membrane potential of CA1 pyramidal cells as head-fixed mice spontaneously alternated between periods of movement and immobility during a spatial navigation task in a virtual reality environment. The $V_m$ of most CA1 pyramidal was modulated during transitions from immobility to movement and vice versa. The majority (~2/3) of CA1 pyramidal cells were hyperpolarized during movement while the remaining cells were depolarized. Hyperpolarization of CA1 pyramidal cells during movement was of high magnitude (~2 mV) and associated with reduced $V_m$ variance and lower firing rates. However, depolarization of CA1 pyramidal cells during movement was more moderate (~0.6 mV), not associated with reduced $V_m$ variance and only slightly higher baseline firing rates. The proportion of hyperpolarized cells during movement (2/3) in our recordings fits well with the proportion of silent cells in a given environment estimated by extracellular as well as intracellular recordings (Thompson and Best, 1989; Wilson and McNaughton, 1993; Epsztein et al., 2011). Thus, a straightforward interpretation of our results is that locomotion-dependent hyperpolarization of a majority of CA1 pyramidal cells in a given environment allows them to stay silent in that environment. In line with this, a recent report highlighted the important role of baseline $V_m$ in controlling place cells activation in a given environment (Lee et al., 2012). In this report a slight depolarization (by a few millivolts) of the baseline $V_m$ of silent pyramidal cells was sufficient to induce a spatially modulated bump of depolarization in these cells and convert them to place cell coding. This suggests that intrinsic properties, and

notably voltage-gated conductance activated below the firing threshold such as $I_{NaP}$ (Hsu et al., 2018) can rapidly convert a silent cell into a place cell. In this framework, most CA1 pyramidal receive spatially modulated inputs but intrinsic conductances, probably in conjunction with specific synaptic inhibition, can gate those inputs in the majority of CA1 pyramidal cells such that only a minority of them (the place cells) can respond to these inputs with spatially modulated firing. In this context, the locomotion-dependent hyperpolarization of the baseline $V_m$ of a majority of CA1 pyramidal cells that we describe could constitute an efficient way to prevent incidental depolarization (and associated place coding) of silent pyramidal cells, thus preserving the sparse coding scheme of the hippocampus. On the other hand, the depolarization of a minority of CA1 pyramidal cells could represent a permissive state for position coding. Alternatively cells hyperpolarized during movement could represent a recently described population of cells that specifically code position during immobility (Kay et al., 2016). We think however that this possibility is unlikely given that immobility place cells represented a small minority of all CA1 pyramidal cells while HypM cells represented the majority of recorded cells in our study. Unfortunately the behavior of the mice and short duration of the recordings prevented the analysis of the spatial modulation of HypM cells' firing. Finally, HypM cells could correspond to transitions from an internal state dominated by large irregular activities (LIA) when CA1 pyramidal cells' $V_m$ is on average more depolarized to theta state when CA1 pyramidal cells' $V_m$ is on average more hyperpolarized (Hulse et al., 2017). However, in this report the authors found no clear changes in $V_m$ or its variability across transitions to theta state and theta periods tended to occur away from identified periods of LIA making this explanation also unlikely. The difference with our results where clear modulation in $V_m$ and its variability (at least for HypM cells) were observed around transitions to movement (an most probably to a theta state)

could lie in the fact that our animals were actively engaged in a spatial navigation task unlike animals in the previous report (see for instance the difference in running speed values).

**Cellular mechanisms of locomotion-dependent bimodal modulation of CA1 pyramidal cells $V_m$**

The bimodal modulation of CA1 pyramidal cells $V_m$ during locomotion could result from locomotion dependent modulation of the excitatory/inhibitory synaptic balance. This balance is however difficult to predict from the existing literature. The overall activity of CA1 pyramidal cells in the hippocampus is reduced during movement compared to periods of quiet wakefulness or during sleep (Kay and Frank, 2017). However, the firing rate of cells active during locomotion is positively modulated by speed (McNaughton et al., 1983; Czurkó et al., 1999). The source of this modulation could be extra-hippocampal. The activity of glutamatergic cells in the medial septum is positively modulated by speed (Fuhrmann et al., 2015). These cells mostly contact interneurons so they could influence pyramidal cells' $V_m$ through feedforward disinhibition. Recent experimental work using juxtacellular recordings followed by post-hoc identification in freely moving rat have observed that PV basket cells but not Ivy cells fire more during movement compared to immobility (Lapray et al., 2012). More recent work using two photon imaging reported that most PV-positive and SOM-positive interneurons' activity is positively modulated by speed (Arriaga and Han, 2017). This is consistent with the speed-dependent hyperpolarization of the majority of recorded CA1 pyramidal cells. However, a small population of interneurons showed an opposite behavior (i.e. their activity was negatively correlated with speed) and could account for the speed dependent depolarization of a minority of recorded CA1 pyramidal neurons in our study.

**Opposite modulation of bursting and regular firing cells during locomotion and functional implications for hippocampal spatial coding**

Intracellular recordings *in vitro* (Graves et al., 2012) and *in vivo* (Kandel and Spencer, 1961; Epsztein et al., 2011) have revealed that CA1 pyramidal cells can respond to intracellularly injected steps of current with two different firing behaviors: firing groups of action potentials with short interspike intervals, also referred to as burst firing cells or action potentials with larger inter-spike intervals also referred to as regular firing cells. *In vitro*, the distribution of burst firing and regular firing CA1 pyramidal cells have been shown to vary along the proximo-distal axis (Jarsky et al., 2008) and to correspond to two different classes of neurons (Graves et al., 2012). Importantly, bursting and regular firing neurons appears to be functionally different (Epsztein et al., 2011; Cembrowski et al., 2018). In freely moving rats, burst firing cells are more readily recruited for spatial coding than regular firing cells when animals explore a new environment (Epsztein et al., 2011). However, the intracellular determinants of place cells coding vary between familiar and new environment with a likely switch from intrinsic to synaptic determinants (Cohen et al., 2017). We observed a preferential locomotion dependent hyperpolarization of bursting CA1 pyramidal cells during locomotion when mice explored a familiar environment while regular firing cells were depolarized. Interestingly, the bursting index, which reflects the propensity of spikes to be fired as bursts in a given cell, correlated with the strength and sign of the modulation. If bursting cells are preferentially recruited to be active and code for position as rats moves around in a new environment, locomotion-dependent hyperpolarization could counter select them to code in a familiar environment. Future work should examine the spatial coding of burst and regular firing cells in a familiar environment as well as the locomotion-dependent modulation of their $V_m$ in a new environment.

Extracellular recordings have also revealed a differential distribution of bursting and regular firing cells along the deep-superficial axis in CA1, with deep cells located close to *stratum oriens* preferentially firing in bursts and superficial cells located close to *stratum radiatum* preferentially firing regularly (Mizuseki et al., 2011). While the link between intrinsic (as determined by intracellular step current injections) and functional (as determined by extracellular recordings of spontaneous firing) bursting properties are currently unknown, it is tempting to speculate that some correspondence exists between these cell classes. Recently, deep CA1 pyramidal cells were shown to be preferentially inhibited during sharp wave ripples (Valero et al., 2015), a behavior that was also observed for HypM bursting cells in the present study whose soma were not located superficially within the CA1 pyramidal cell layer. Interestingly, a recent report have shown that deep and superficial cells are differently engaged in spatial coding depending on the type of information available to the animal (Fattahi et al., 2018). Deep cells are recruited to code positions close to external landmark cues (Geiller et al., 2017) when coding can rely on allothetic information while superficial cells are recruited to code positions away from landmarks when coding must rely on idiothetic information (Fattahi et al., 2018). The opposite membrane potential modulation during locomotion between burst firing and regular firing cells could also provide a mean to differently recruit deep and superficial cells for spatial coding depending on external cues available for self-location.

# Material and methods

## Animals

All the experiments have been approved by the Institut National de la Santé et de la Recherche Médicale (INSERM), animal care and use commitee and authorized by the Ministère de l'Education Nationale de l'Enseignement Supérieur et de la Recherche (agreement n° 02048.02), in agreement with the directives of the European Community Council (2010/63 / EU). Data were acquired on 13 C57BL6 mice and 1 CD-1 mouse aged from five to eight weeks weighting between 18 g and 28 g at the first surgery. The mice were housed 2 or 3 per cages before the first surgery and then individually with 12h inverted light/dark cycles. Trainings and recordings occurred during the dark phase. Water and food have been provided *ad libitum* upstream of the surgeries. After recovery from the first surgery, the mice were restricted to 1 ml/day of water and their weight and health were monitored daily during the following experiments.

## Surgery

A first surgery is performed to implant a fixation bar used later for the fixation of the head. The animals were anesthetized with induction of 3% isoflurane followed by an intraperitoneal injection of Ketamine (100 mg/kg) mixed with Xylazine (10 mg/kg) supplemented with subcutaneous Buprenorphine injection (0.06 mg/kg). Jeweler's screws were inserted into the skull above the cerebellum and above the olfactory bulbs to anchor dental cement. A dental cement cap was then constructed leaving two areas of the skull free to subsequently perform the craniotomies necessary for registration (in reference to Bregma: Antero-Posteriority (AP): -2mm, Medio-Laterality (ML): -2.2) for the first target

necessary for intracellular recording and AP: -3mm and ML: -3.1 for the second target necessary for LFP recordings). In 4/14 mice, a LFP electrode (coated tungsten wire) was placed with an angle of 45° on z axis of an orthogonal reference frame and 45° on x axis until reaching the CA1 pyramidal layer determined by the presence of sharp wave-ripples. The electrode was then fixed with dental cement. The cement-free skull was coated with a 2% agarose layer and sealed with silicon elastomer (Kwik-Cast, World Precision Instruments). A small titanium bar (0.65 g, 12 x 6 mm) was subsequently inserted into the dental cement cap above the cerebellum. This bar is continuously present on the animals head and will serve as a point of attachment to a larger metal plate used only during training and recordings for fixing the head of the animals on the virtual reality device.

**Virtual reality set up**

A commercially available virtual reality system (Phenosys Jetball-TFT) was combined with a custom designed 3D printed concave plastic wheel (center diameter: 12.5 cm; side diameter: 7.5 cm; width: 14 cm, covered with silicon-based white coating) to allow 1D movement with a 1/1 coupling between the movements of the mouse on the wheel and the movements of its avatar in the virtual reality environment. The plastic wheel was preferred to the original ball which had a more variable coupling due to its lateral rotations. The movement information is transmitted to the computer which subsequently updates the position of the avatar in the virtual environment. The wheel was surrounded by six 19-inch TFT monitors covering a 270-degree angle (Fig.S1A). The monitors were put up so that the level of mouse's eyes corresponded to the lower third of the height of the screen. This elevation was made to take into account that the field of view of rodents is generally oriented upwards. A head fixation system (Luigs and Neumann) was located behind the animal to avoid interfering with

the display of the virtual reality environment. The movement of the wheel updated the position of the mouse. The mouse could only move forward or backward but could not go back to the middle of the track (see training section).

**Virtual Environments**

The environment used for trainings (10/14 mice, 13/17 cells) and during recording sessions (14/14 mice, 17/17 cells) was a 200-cm long and 32-cm wide virtual corridor composed of four successive symmetrical and distinct patterns (respectively black dots on a white background, black and green squares, black and white strips, green crosses on a black background) with two target images at the ends (gray circles on a yellow background and triangles on a yellow background; Fig.S1B,C). Three objects were present in the environment: a yellow origami crane (dimensions: 9 x 9 x 7 cm: position: 37 cm from the beginning of the corridor), a gray cube with a blue diamond pattern (dimensions: 5 x 5 x 5 cm, position: 64 cm from the beginning of the corridor) and a tree (dimensions: 15 x 15 x 22 cm, position: 175 cm from the beginning of the corridor), as well as symmetrical columns present outside the corridor (dimensions: 8 x 8 x 47 cm, positions from the beginning of the corridor: 58 and 143 cm, patterns: black rhombus on green background, black and white horizontal stripes). For five recordings, after exploration of this previous maze, mice were teleported in the same version of that maze except for objects in the environment which were removed from it. Four mice were trained in a virtual maze which was empty except a black and grey rhombus floor pattern and with a green circle place at 200 cm on the ground indicating the reward zone.

**Habituation and trainings**

The mice were first habituated to the experimenter by at least two daily manipulation sessions of at least 20 minutes which continued throughout the experiment. After a period of post-operative recovery of at least 3 days, mice were restricted to water (1 ml/day, including the amount of water taken during training) and their weight was controlled daily. Access to *ad libitum* water was restored if the weight of the animals decreased by less than 80% of the pre-operative weight at any stage of training. Then, after 2 or 3 days of water deprivation, they were gradually trained to run in the virtual reality device. In first place, mice became familiar with the device by being head fixed on the wheel in a black virtual environment where it is possible to recover sweet water rewards (5%) of 8 µl every 50 cm. Following at least one training in the black environment, the animals were trained to run in the virtual environment described in the previous section. When an animal reaches the end of the labyrinth, a sweet water reward of 5% of 8 µl is given *via* an arm that unfolds and a pump controlled by a tactile licking sensor. Once the reward is taken by the animal, the arm returns to its original position and the avatar is teleported in the opposite direction until the next reward at the end of the corridor. Animals were initially trained during 10 minutes daily sessions in the environment with periods of breaks in a black environment without any task. During training, the time in the black environment was gradually increased to 60 minutes in order to better mimic the recording conditions.

**Recording procedures**

When animals reached stable behavioral performances in the training maze (at least 6 training sessions and at least 1 session with 1.2 reward/minute performance), we performed intracellular recordings of hippocampal pyramidal cells as well as a recording of hippocampal

field using either a wire placed during initial surgery or a linear silicon probe (A-32 Buzsaki Probe, Neuronexus) with 32 recordings channels spaced with 25 or 50 µm placed during recording day. For 2/17 recorded cells, LFP recordings were too noisy to be analyzed. The day before the recording, animals were anesthetized (induction: isoflurane 3%, maintenance with sleep mix: medetomidine (225 mg/kg), midazolam (6 mg/kg), and fentanyl (7.5 mg/kg), awaken with awake mix: atipamezole (1 mg/kg), flumazenil (600 mg/kg), and naloxone (180 mg/kg)) and craniotomies were performed. Craniotomies were covered with agarose (~ 3% in saline) and then sealed with silicon elastomer (Kwik-Cast, World Precision Instruments). On the day of recording, the back of the silicon probe was covered with a thin layer of a red fluorescent dye (DiI, Life Technologies) so that the recording location was evaluated post-hoc histologically. The silicon probe was then descended in the brain with an angle of 45° on the z axis of an orthogonal reference frame and 45° on the x axis while the animal could move freely on the wheel with the screens displaying a black environment. The correct positioning of the probe in the pyramidal cell layer CA1 was verified by the presence of sharp-wave ripples during the stop of the animal on several channels. From the depth of CA1, the probe was then lowered with an additional 600-1100 µm depth in order to reach other structures such as the dentate gyrus and CA3. After positioning the silicon probe, the intracellular recordings were performed.

Patch pipettes were made and visually checked the same morning of recording sessions. The average resistance of the pipettes was between 5 and 8 MOhm and was filled with an intracellular solution containing (in mM) K-gluconate: 135, HEPES: 10, Na2-phosphocreatine: 10, KCl: 4, MgATP: 4, and Na3GTP: 0.3 (pH adjusted to 7.2), plus biocytin (0.05%) to allow the revelation of the recorded cells. The very first pipette of a recording session was filled with an extracellular medium (Ringer) and descended above the hippocampus to estimate the

depth of the CA1 layer (based on observation in the signal "sharp-wave ripples" during immobility). Once the CA1 depth was estimated, other pipettes were lowered into a voltage clamp configuration with a pulse of 10 mV at 20 Hz and a high pressure (> 400 mmpA) to reach arround -100 µm ahead the estimated depth of CA1. The pressure of the pipettes was then decreased to ~30 mmPA to allow clamping of the cells. If a recording pipette was clogged during the descent, it was replaced. Once the GΩ seal was obtained, a cell was opened by a negative pressure deflection to go into full cell configuration and the recording was set in a current clamp configuration. A discharge pattern was executed (current steps starting from -400 pA with an increment of 50 pA) upstream of each record in the virtual environment. Once the discharge pattern was performed, the virtual environment described previously was displayed and animals went back and forth. For 9/17 recordings, hyperpolarizing steps of current were injected (-100 pA) every 40 s during exploration. In case of failure of GΩ-seal or loss of the cell, the pipette was changed and the procedure was repeated.

**Data acquisition**

The position of the animal in the virtual environment was digitized by the computer controlling the virtual reality (Phenosys) and sent to a digital - analogue card (0-4.5V, NI USB-6008 National Instrument Map) connected to a specialized acquisition card for intracellular recordings (molecular device, Digidata 1550A) and also connected to an external analog card (I / O card, Open Ephys) of a 256-channel acquisition card (Open Ephys) specialized in multi-channel probe recording.

The Open Ephys system and linear silicon probe recordings were not available during the first recordings present in this study so initial recordings (4/14 mice, 6/17 recorded cells) were carried out on continuous signals acquired on the molecular device card, Digidata 1550A with a frequency of acquisition of 20 kHz. For other recordings (10/14 mice, 11/17 recorded cells), electrophysiological signals were acquired on Open Ephys card at an acquisition frequency of 25 kHz (Open Ephys, Intan Technologies, RHD2132 amplifier with a RHD2000 USB card).

**Histological revelation, labelling and reconstruction:**

Biocytin revelation: After patch recording sessions, all animals were perfused with 4% PFA and brains were collected to put in a 4% PFA solution during 24h - 48h (depending on state of perfusion), then transferred in a 1X PBS solution before being sliced with 50-100 µm thickness. All animals received protocol of biocytin revelation. Biocytin was revealed by an incubation of streptavidin coupled with an Alexa 594 fluorophore (10/14 animals) or coupled with cyanin 3 (4/10 animals) at 1/1000 concentration in mix of 1X PBS, 0.3% triton and 2% Normal Goat Serum (NGS) (in order to permeabilize membranes and reduces nonspecific liaisons) under agitation at 4°C protected from light during 48h-72h. Slices were then washed during 10 minutes 3 times under agitation protected from light at 4°C with 1X PBS. Localization of labelled cells was determined with an Olympus SZX 16 stereomicroscope. Slice within the soma of labeled cell, as well as 2 slices before and 2 slices after, were identified and received calbindin positive labeling protocol (12/14 animals, 14/17 cells).

Calbindin labelling: Interest slices were incubated with a mix of 1X PBS, 0.3% triton and 7% NGS, during 2h at 4°C protected from light. Then, slices were incubated and agitated during

24h at 4°C protected from light with a primary rabbit antibody anti-calbin at 1/1000 in a mix of 1X PBS, 0.3% triton, 2% NGS added with streptavidin coupled with a fluorophore at 1/1000 (Alexa 594 or cyanine 3) in order to maintain labeling of biocytin. After 3 washes of 10 min in a mix of 1X PBS and triton 0.3%, slices were then incubated and agitated during 24h at 4°C protected from light with a secondary donkey antibody anti-rabbit coupled with Alexa 488 fluorophore at 1/1000 in mix of 1X PBS, 0.3% triton, 2% NGS added with streptavidin coupled with a fluorophore at 1/1000 (Alexa 594 or cyanine 3). Finally, slices were washed during 10min 3 times in a mix of 1X PBS and 0.3% triton with agitation at 4°C protected from light and then 2 more washes with only 1X PBS in the same condition. Slices were then mounted between blades and coverslips using Vectashield (containing DAPI) and then sealed with uncolored nail polish.

Microscope & reconstruction: 6 brains were acquired using Leica SP5X streptal microscope in order to reconstruct labelled cells. Acquisition was made with a resolution of 2048 x 2048 using a x40 lens and done with stacks 0.46 µm of thickness. 2 fully labelled neurons were reconstructed thanks to Neurolucida® software (Fig. S4). These two neurons were also acquired with a x10 lens for a wide view and x40 for an isolated view of the neuron using a Zeiss LSM 800 microscope.

**Data Analysis**

Analyzes were performed by custom developed programs written in MATLAB (MathWorks). 17 cells were recorded with duration from 1 to 23 min in the maze (mean: 8 min 25 s ± 1 min 34 s). Animals performed at least one lap in the environment (mean: 6.82 ± 1.3).

Intrinsic properties: Intrinsic properties features comes from pattern discharge executed before exploration of the environment. The resting membrane potential of the cells was determined as the average of the first 15 milliseconds of the recording. Series and the input resistances were calculated by fitting a linear curve on all the hyperpolarizing and depolarizing current steps excluding steps with action potentials. The discharge threshold has been recovered on the first action potential emitted by the cell in response to a minimum current. It was defined as the value of the membrane potential where the derivative of the signal exceeded 10 $mV.s^{-1.}$ The spike amplitude was calculated as the difference between peak of this first action potential and the threshold. The Rheobase was calculated by fitting a linear regression curve on the firing frequency depending on steps of current. The value taken was the theoretical minimal injection of current needed to evoke one spike. Rheobase values were then validated manually if aberrant values were found by the fit (11/17 values kept). The bursting index was calculated on the first current step with at least 5 action potentials (AP) and by calculating the ratio of the number of action potential discharging in bursts (PA with an inter-potential interval less than 10 ms) over the total number of action potential present during the pulse.

Subthreshold $V_m$: Subthreshold $V_m$ has been determined using the following steps. First, a window of stable $V_m$ were selected on recorded cells. Artifacts (aberrant loss of signal) were manually selected and removed by linearizing the $V_m$ between edges (9/17 recordings). Influence of series resistance on $V_m$ was automatically corrected following the Ohm law $U = R_s.I$, based on series resistance values taken from intrinsic properties. Action potentials from $V_m$ were detected automatically using a high pass filter (100 Hz) and an adjustable threshold

equal to 4 times the $V_m$ standard deviation (s.d.). Good detection of spikes was then checked manually. Edges of spikes were defined as 2 ms before and 8 ms after action potential peak. Complex spikes from $V_m$ were detected using different filters and thresholds. A vector was computed in order to detect slow component of a complex spike. This vector corresponds to a band pass filtered $V_m$ (0.5-20 Hz), which positive values were squared. The final vector was z-scored. Putative indexes of complex spike were detected using 2 thresholds. A first threshold was equal to 10 (value of z-score) and then extended using a lower threshold equal to 5 when the difference between both threshold indexes did not exceed 30 ms. Short detected events inferior to 30 ms were then removed. Next, edges of putative events were asymmetrically extended by 25 ms before and 4 ms after putative complex spikes. Finally, all putative complex spikes edges were checked and manually corrected if needed. Spikes and complex spikes were removed by linearizing the $V_m$ between edges of events. Small $V_m$ drift was compensated using a low pass filter (0.1 Hz) in order to realign $V_m$. Hyperpolarizing steps of current were automatically detected on the current trace and removed from the $V_m$ trace by linearizing. Current trace was first filtered at 1 Hz, then indexes were found by using a threshold equal to 5 times the standard deviation of the current trace. Only periods < 200 ms were included. Indexes separated by less than 40 ms were merged. Finally indexes were extended with 10 ms before and 40 ms after edges of detected periods.

<u>Locomotion/immobility periods:</u> To detect locomotion and immobility periods, the velocity vector was calculated on the signal position in the environment (6/17 recordings) or, when available, directly on the signal of the motion sensor downsampled at 100 Hz and then smoothed (11/17 recordings). The speed corresponds to the derivative of the smoothed

position vector then smoothed again with a half-width Gaussian of 0.5 s. Because the reward system freezes the virtual environment in the reward zone but did not physically stop the wheel on which the animal is walking, rewards zone were excluded from the analysis when the wheel movement signal was not available. Putative periods of locomotion and immobility were detected by applying a speed threshold of 0.5 $cm.s^{-1}$. Then, periods separated by less than 0.5 s have been merged. Finally, only periods greater than or equal to 2 s have been preserved, others were unlabeled. Transitions periods were defined as periods centered on the index for which the animal went from immobility to locomotion or vice versa. Transitions had a total duration of 4 s (2 s immobility and 2 s locomotion).

Subthreshold $V_m$ features during Locomotion/Immobility: Mean subthreshold $V_m$, subthreshold $V_m$ variance and mean spontaneous firing rate were calculated for each locomotion/immobility period. To be able to compare the $V_m$ of different neurons, the Z-score was computed on the subthreshold $V_m$. Intracellular spectrogram was computed by using a time-frequency decomposition with complex Morlet wavelets with central frequencies from 0 to 40 Hz in 0.2 Hz steps on a downsampled signal (250 Hz). Power values in a given frequency range were normalized by the squared root of the frequency. Then mean power values were calculated during immobility and locomotion periods. For scatterplots in Fig.1 and Fig.2, only successive periods of immobility and movement were considered in order to be able to plot values face to face in scatter plots. For the supplementary figure 3, scatter plots during transitions periods come from values between -2 s and -1 s versus values between +1 s and +2 s (0 s being the center of the transition).

608 Modulation index computation: Cells were classified as Depolarized (Dep M) or
609 hyperpolarized (Hyp M) during locomotion depending on a subthreshold $V_m$ modulation
610 index. This index was calculated by counting for each period of locomotion occurring before
611 or after a given period of immobility the percentage of $V_m$ values higher than the median of
612 the $V_m$ during the immobility period. 750 ms before and after each locomotion/immmobility
613 was removed to compute this index. The percentage has been rescaled to get an index from
614 -1 to 1 used to classify DepM and HypM cells.

615

616 Speed correlation: Z-score Subthreshold $V_m$ trace was filtered with a lowpass filter at 5Hz,
617 then downsampled at 100Hz and smoothed with a half-width Gaussian of 1 sec. Next, for
618 each neuron a correlation coefficient was computed by calculating the correlation
619 coefficient between averaged Z-score Subth. $V_m$ values and Speed vector binned in 0.05
620 cm.s-1 bins containing at least 4 values. For each neuron a mean coefficient correlation was
621 also calculated based on the mean of correlation coefficient during each moving periods.

622

623 Ripples detection: Ripples were detected on the CA1 LFP signal when available (15/17
624 recordings) during immobility. To detect ripples, LFP signal was filtered between 100Hz
625 and 300Hz, then squared and smoothed with an half Gaussian of 10 ms and finally z-scored.
626 Putative indexes of ripples were detected using 2 thresholds. A first threshold was equal to 5
627 times the s.d. of the signal and then extended using a lower threshold equal to 2 times the
628 signal s.d. when the difference between both threshold indexes did not exceed 18 ms. Then
629 putative ripples periods were merged if they were separated by an amount of time inferior
630 to 30 ms. Next, periods of ripples were extended by 5 ms in each direction and then, a time

restriction was applied in order to conserve only putative periods of at least 25 ms. Finally, putative periods of ripples were then checked manually and time of occurrence of ripple was taken as the index of maximum of signal in the ripple period.

Ripples modulation features computation: Subthreshold $V_m$ modulation by ripples was computed by using a shuffling method repeated 1000 times. At each iteration, a randomized vector was calculated by shuffling the subthreshold $V_m$ values within a time window from 2 times the length of the ripple before its start to the end of the ripple. Then the number of times where subthreshold $V_m$ was superior or inferior of randomized vector was counted. If the subthreshold Vm is superior of inferior to 95% of the 1000 randomized vectors for 10% of the ripple period duration, then the modulation of the $V_m$ by the ripple was considered as significant. Baseline used to calculate Delta$V_m$ modulation during ripple was calculated as the mean of Subthreshold $V_m$ within a time window from 2 times the length of ripple to its start. Delta $V_m$ was computed as the maximum or minimum significant subthreshold $V_m$ value minus the Baseline. If two significant $V_m$ modulations were present in one ripple period, the first one occurring was taken to calculate the Delta$V_m$.

Statistical analysis: All statistical analyses were conducted using Matlab codes (MathWorks). For each distribution, a Lilliefors goodness-of-fit test was used to verify if the data were normally distributed and a Levene test was used to assess for equal variance. If normality or equal variance were not verified, we used the Wilcoxon rank sum test otherwise the Student t-test was used. For paired test, normality was verified by Lilliefors goodness-of-fit test. If

normality was not verified, we used the Wilcoxon signed rank test otherwise the Student paired t-test. In figure or text, all results were given with means ± the s.e.m..

# References


Albergaria C, Silva NT, Pritchett DL, Carey MR (2018) Locomotor activity modulates associative learning in mouse cerebellum. Nat Neurosci 21:725-735.

Arriaga M, Han EB (2017) Dedicated Hippocampal Inhibitory Networks for Locomotion and Immobility. J Neurosci 37:9222–9238.

Arroyo S, Bennett C, Hestrin S (2018) Correlation of Synaptic Inputs in the Visual Cortex of Awake, Behaving Mice. Neuron 99:1289–1301.

Bennett C, Arroyo S, Hestrin S (2013) Subthreshold mechanisms underlying state-dependent modulation of visual responses. Neuron 80:350–357.

Bittner KC, Grienberger C, Vaidya SP, Milstein AD, Macklin JJ, Suh J, Tonegawa S, Magee JC (2015) Conjunctive input processing drives feature selectivity in hippocampal CA1 neurons. Nat Neurosci 18:1133–1142.

Buzsaki G (1989) Two-stage model of memory trace formation: a role for "noisy" brain states. Neuroscience. 31:551-570.

Buzsáki G (2015) Hippocampal sharp wave-ripple: A cognitive biomarker for episodic memory and planning. Hippocampus 25:1073–1188.

Buzsáki G, Horváth Z, Urioste R, Hetke J, Wise K (1992) High-frequency network oscillation in the hippocampus. Science 256:1025-1027.

Cembrowski MS, Phillips MG, DiLisio SF, Shields BC, Winnubst J, Chandrashekar J, Bas E, Spruston N (2018) Dissociable Structural and Functional Hippocampal Outputs *via* Distinct Subiculum Cell Classes. Cell 173:1280–1292.

Cohen JD, Bolstad M, Lee AK (2017) Experience-dependent shaping of hippocampal CA1 intracellular activity in novel and familiar environments. Elife 6:1–27.

Colgin LL (2016) Rhythms of the hippocampal network. Nat Rev Neurosci 17:239–249.

Crochet S, Petersen CCH (2006) Correlating whisker behavior with membrane potential in barrel cortex of awake mice. Nat Neurosci. 9:608-610.

Czurkó A, Hirase H, Csicsvari J, Buzsáki G (1999) Sustained activation of hippocampal pyramidal cells by 'space clamping'in a running wheel. Eur J Neurosci 11:344–352.

English DF, Peyrache A, Stark E, Roux L, Vallentin D, Long MA, Buzsáki G (2014) Excitation and Inhibition Compete to Control Spiking during Hippocampal Ripples: Intracellular Study in Behaving Mice. J Neurosci 34:16509–16517.

Epsztein J, Brecht M, Lee AK (2011) Intracellular Determinants of Hippocampal CA1 Place and Silent Cell Activity in a Novel Environment. Neuron 70:109–120.

Epsztein J, Lee AK, Chorev E, Brecht M (2010) Impact of spikelets on hippocampal CA1 pyramidal cell activity during spatial exploration. Science 327:474–477.

Fattahi M, Sharif F, Geiller T, Royer S (2018) Differential Representation of Landmark and Self-Motion Information along the CA1 Radial Axis: Self-Motion Generated Place Fields Shift toward Landmarks during Septal Inactivation. J Neurosci 38:6766–6778.

Foster DJ, Wilson MA (2006) Reverse replay of behavioural sequences in hippocampal place cells during the awake state. Nature 440:680-683.

Fuhrmann F, Justus D, Sosulina L, Kaneko H, Beutel T, Friedrichs D, Schoch S, Schwarz MK, Fuhrmann M, Remy S (2015) Locomotion, Theta Oscillations, and the Speed-Correlated Firing of Hippocampal Neurons Are Controlled by a Medial Septal Glutamatergic Circuit. Neuron 86:1253–1264.

Gan J, Weng S ming, Pernía-Andrade AJ, Csicsvari J, Jonas P (2017) Phase-Locked Inhibition, but Not Excitation, Underlies Hippocampal Ripple Oscillations in Awake Mice In Vivo. Neuron 93:308–314.

Geiller T, Fattahi M, Choi JS, Royer S (2017) Place cells are more strongly tied to landmarks in deep than in superficial CA1. Nat Commun 8:14531.

Girardeau G, Zugaro M (2011) Hippocampal ripples and memory consolidation. Curr Opin Neurobiol 21:452–459.

Graves AR, Moore SJ, Bloss EB, Mensh BD, Kath WL, Spruston N (2012) Hippocampal Pyramidal Neurons Comprise Two Distinct Cell Types that Are Countermodulated by Metabotropic Receptors. Neuron 76:776–789.

Grienberger C, Milstein AD, Bittner KC, Romani S, Magee JC (2017) Inhibitory suppression of heterogeneously tuned excitation enhances spatial coding in CA1 place cells. Nat Neurosci 20:417–426.

Gupta AS, van der Meer MAA, Touretzky DS, Redish AD (2010) Hippocampal Replay Is Not a Simple Function of Experience. Neuron 65:695-705.

Harvey CD, Collman F, Dombeck DA, Tank DW (2009) Intracellular dynamics of hippocampal place cells during virtual navigation. Nature 461:941–946.

Hsu CL, Zhao X, Milstein AD, Spruston N (2018) Persistent Sodium Current Mediates the Steep Voltage Dependence of Spatial Coding in Hippocampal Pyramidal Neurons. Neuron 99:147–162.

Hulse BK, Lubenov E V., Siapas AG (2017) Brain State Dependence of Hippocampal Subthreshold Activity in Awake Mice. Cell Rep 18:136–147.

Hulse BK, Moreaux LC, Lubenov E V., Siapas AG (2016) Membrane Potential Dynamics of CA1 Pyramidal Neurons during Hippocampal Ripples in Awake Mice. Neuron 89:800–813.

Jarsky T, Mady R, Kennedy B, Spruston N (2008) Distribution of bursting neurons in the CA1 region and the subiculum of the rat hippocampus. J Comp Neurol 506:535–547.

Kandel ER, Spencer WA (1961) Electrophysiology of hippocampal neurons: II. After-potentials and repetitive firing. J Neurophysiol 24:243–259.

Kay K, Frank LM (2018) Three brain states in the hippocampus and beyond. Hippocampus. In press.

Kay K, Sosa M, Chung JE, Karlsson MP, Larkin MC, Frank LM (2016) A hippocampal network for spatial coding during immobility and sleep. Nature 531:185–190.

Lapray D, Lasztoczi B, Lagler M, Viney TJ, Katona L, Valenti O, Hartwich K, Borhegyi Z, Somogyi P, Klausberger T (2012) Behavior-dependent specialization of identified hippocampal interneurons. Nat Neurosci 15:1265–1271.

Lee D, Lin BJ, Lee AK (2012) Hippocampal place fields emerge upon single-cell manipulation of excitability during behavior. Science 337:849–853.

McGinley MJ, David S V., McCormick DA (2015) Cortical Membrane Potential Signature of Optimal States for Sensory Signal Detection. Neuron 87:179-192.

McNaughton BL, Barnes CA, O'Keefe J (1983) The contributions of position, direction, and velocity to single unit activity in the hippocampus of freely-moving rats. Exp Brain Res. 52:41-49.

Mizuseki K, Diba K, Pastalkova E, Buzsáki G (2011) Hippocampal CA1 pyramidal cells form functionally distinct sublayers. Nat Neurosci 14:1174–1183.

Moser EI, Moser M-B, McNaughton BL (2017) Spatial representation in the hippocampal formation: a history. Nat Neurosci 20:1448–1464.

Niell CM, Stryker MP (2010) Modulation of Visual Responses by Behavioral State in Mouse Visual Cortex. Neuron 65:472-479.

O'Keefe J, Dostrovsky J (1971) The hippocampus as a spatial map. Preliminary evidence from unit activity in the freely-moving rat. Brain Res 34:171–175.

O'Keefe J, Nadel L (1978) The hippocampus as a cognitive map. London: Oxford University Press.

Pfeiffer BE, Foster DJ (2013) Hippocampal place-cell sequences depict future paths to remembered goals. Nature 497:74–79.

Polack PO, Friedman J, Golshani P (2013) Cellular mechanisms of brain state-dependent gain modulation in visual cortex. Nat Neurosci 16:1331–1339.

Roumis DK, Frank LM (2015) Hippocampal sharp-wave ripples in waking and sleeping states. Curr Opin Neurobiol 35:6–12.

Rowland DC, Yanovich Y, Kentros CG (2011) A stable hippocampal representation of a space requires its direct experience. Proc Natl Acad Sci 108:14654–14658.

Thompson LT, Best PJ (1989) Place Cells and Silent Cells in the Hippocampus Rats of. J Neurosci 9:2382–2390.

Valero M, Cid E, Averkin RG, Aguilar J, Sanchez-Aguilera A, Viney TJ, Gomez-Dominguez D, Bellistri E, De La Prida LM (2015) Determinants of different deep and superficial CA1 pyramidal cell dynamics during sharp-wave ripples. Nat Neurosci 18:1281–1290.

Vanderwolf CH (1969) Hippocampal electrical activity and voluntary movement in the rat. Electroencephalogr Clin Neurophysiol. 26:407-418.

809 Vinck M, Batista-Brito R, Knoblich U, Cardin JA (2015) Arousal and Locomotion Make Distinct
810 Contributions to Cortical Activity Patterns and Visual Encoding. Neuron 86:740–754.
811
812 Wilson M, McNaughton B (1993) Dynamics of the hippocampal ensemble code for space. Science
813 (80- ) 261:1055–1058.
814

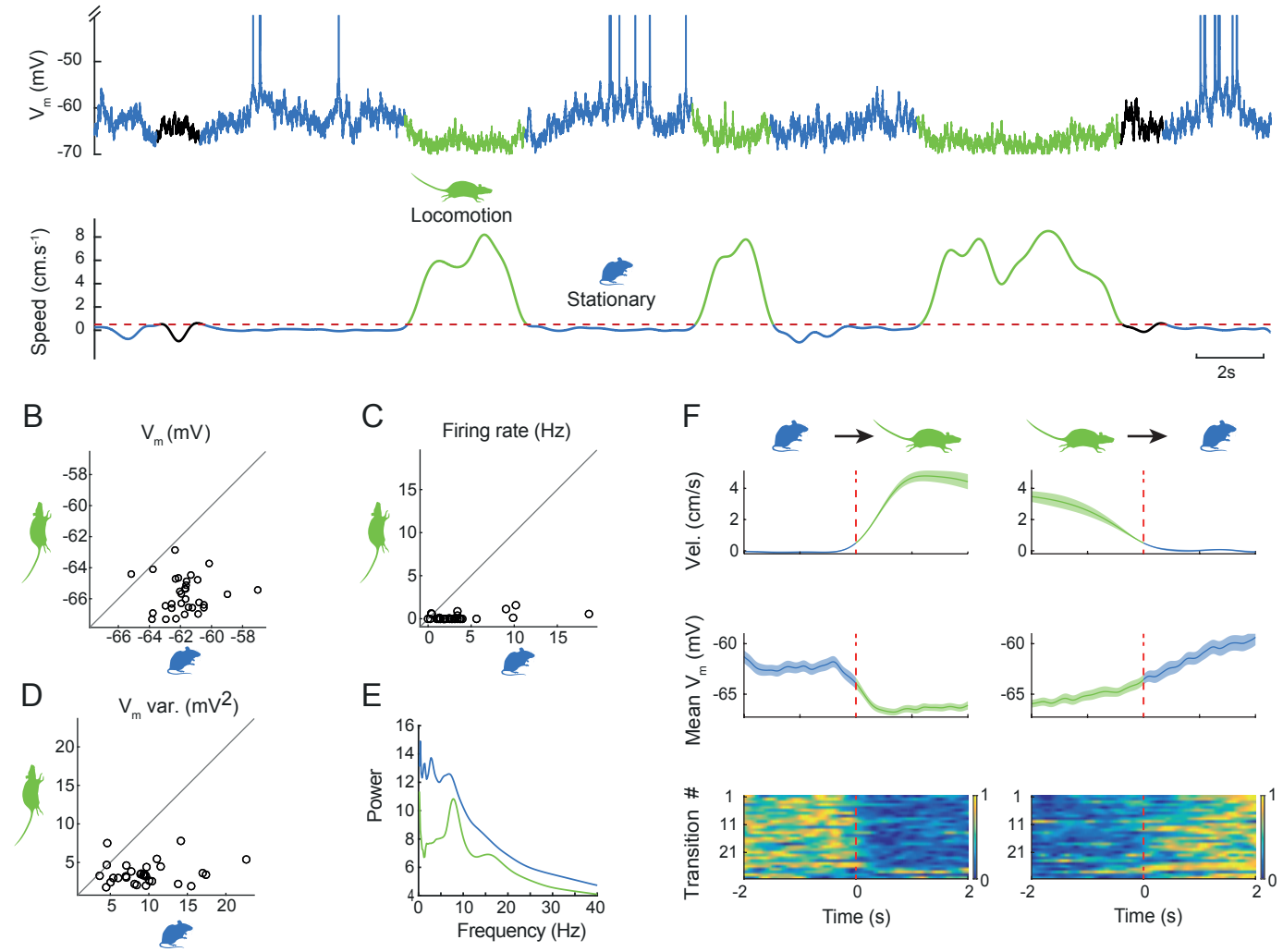


**Fig.1 Hyperpolarized cell during movement:**

**A.** Trace of the $V_m$ and speed of an animal during movement (green), during immobility (blue) or during an unaffected state (black) in a CA1 pyramidal cell recording. In the $V_m$ trace, action potentials have been truncated to highlight subthreshold $V_m$ changes during movement. **B.** Scatterplot of subthreshold $V_m$ during movement versus immobility periods, each point correspond to mean value of one period **C.** Scatterplot of mean firing frequency during movement versus immobility periods. **D.** Scatterplot of mean subthreshold $V_m$ variance during movement versus immobility periods. **E.** Intracellular power spectrum during movement (green) and immobility (blue) periods. **F.** top to bottom : mean velocity, mean subthreshold $V_m$ and normalized subthreshold $V_m$ of each transition during initiation of movement (left) and for the stop of movement (right)

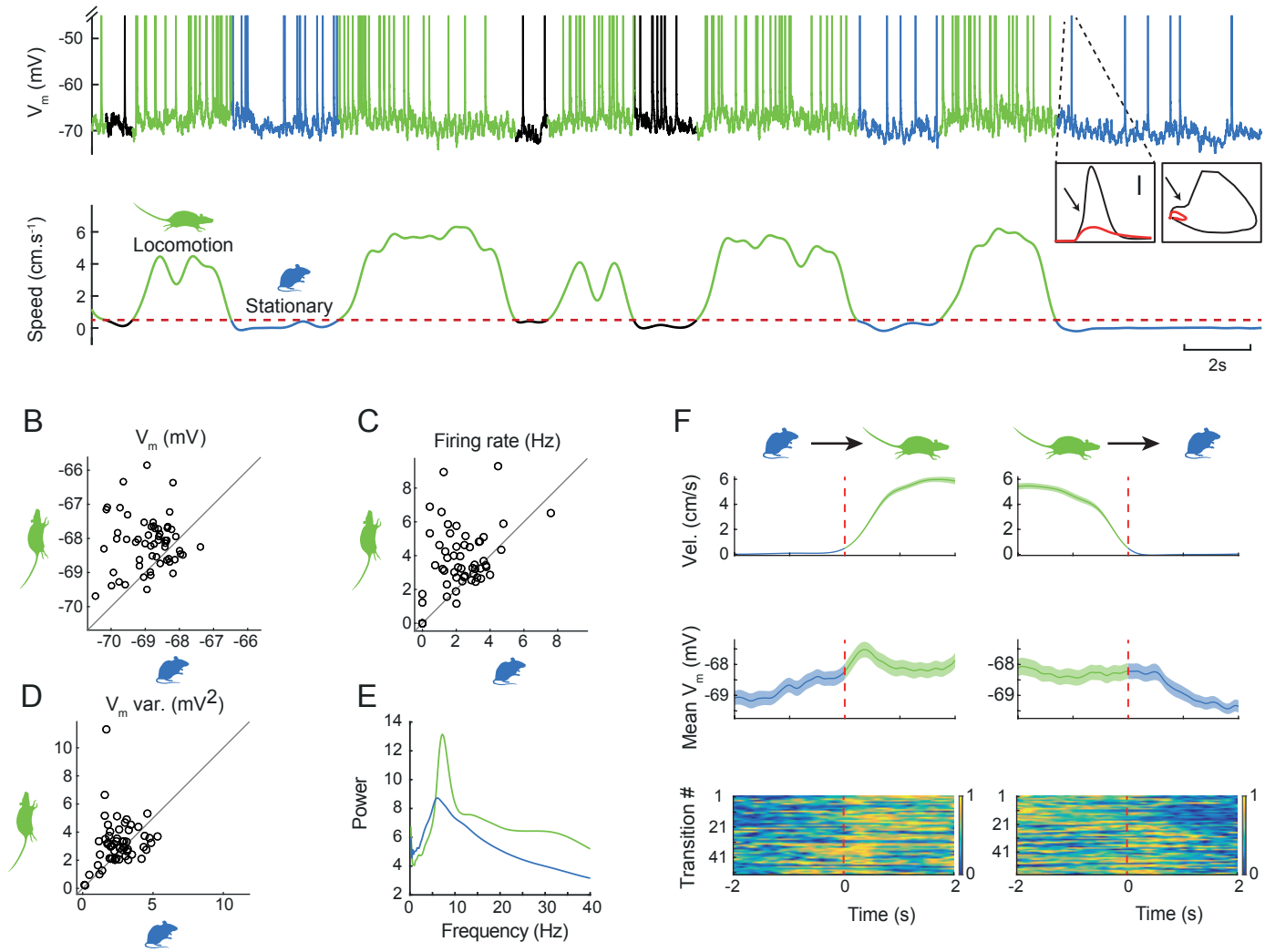


**Fig.2 Depolarized cell during movement:**

**A.** Trace of the $V_m$ and speed of an animal during movement (green), during immobility (blue) or during an unaffected state (black) in a CA1 pyramidal cell recording. In the $V_m$ trace, action potentials have been truncated to highlight subthreshold $V_m$ changes during movement. Magnification: one action potential (black) and a superposed spikelet (red) and associated phase plot, bar = 20mV. In this recording, most of action potentials were generated due to spikelets. **B.** Scatterplot of subthreshold $V_m$ during movement versus immobility periods, each point correspond to mean value of one period **C.** Scatterplot of mean firing frequency during movement versus immobility periods. **D.** Scatterplot of mean subthreshold $V_m$ variance during movement versus immobility periods. **E.** Intracellular power spectrum during movement (green) and immobility (blue) periods. **F.** top to bottom : mean velocity, mean subthreshold $V_m$ and normalized subthreshold $V_m$ of each transition during initiation of movement (left) and for the stop of movement (right)

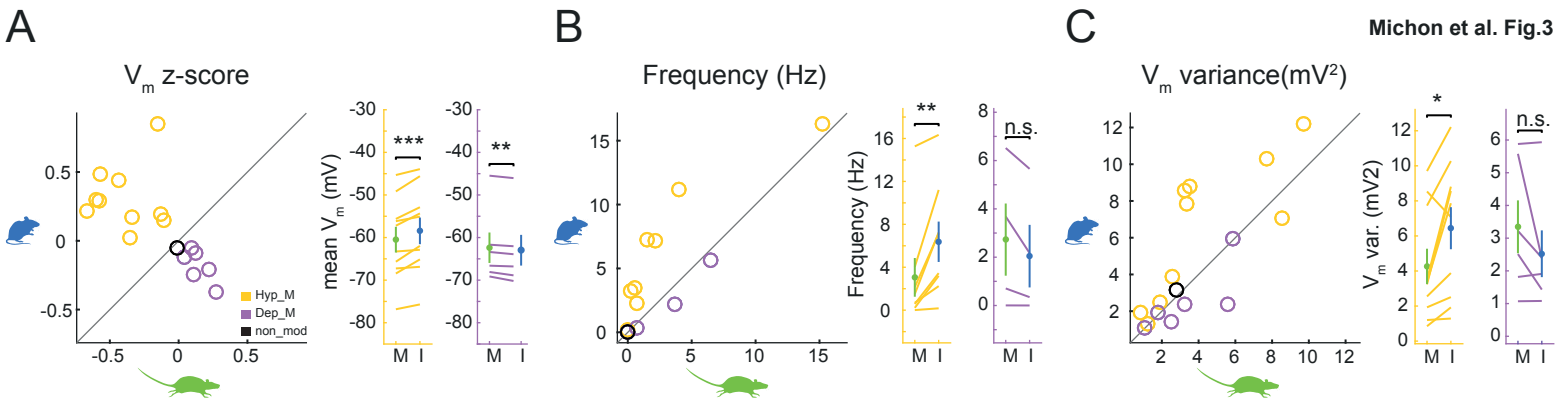


**Fig.3 Opposite modulation of subth.Vm during movement**

**A.** Left: Mean subthreshold $V_m$ during movement versus immobility of hyperpolarized cells (Hyp M group, in yellow), depolarized cells (Dep M group in purple) and non modulated cells (black) during movement. Right: Mean subthreshold $V_m$ during movement versus immobility of Hyp M cells ( $\Delta$ = -2.07 ± 0.42 mV, n=10, p= $7.88.10^{-4}$, paired t-test) and Dep M cells ($\Delta$ = 0.58 ± 0.13 mV , n=6, p= 0.006, paired t-test). **B.** Left: Same as A for the firing frequency; cells that are totally silent during movement and during immobility were removed. Right : Mean firing frequency during movement versus immobility of Hyp M cells ($\Delta$ = -3.32 ± 0.87 Hz, n=8, p=0.006, paired t-test) and Dep M cells ($\Delta$ = 0.68 ± 0.33 Hz, n=4, p= 0.128, paired t-test). **C.** Left : Same as A and B for the subthreshold $V_m$ variance. Right: Mean subthreshold $V_m$ variance during movement versus immobility of Hyp M cells ($\Delta$ = -2.18 ± 0.72 $mV^2$ , n=10, p= 0.015, paired t-test) and Dep M cells ($\Delta$ = 0.82 ± 0.52 $mV^2$ , n=6, p= 0.171, paired t-test).

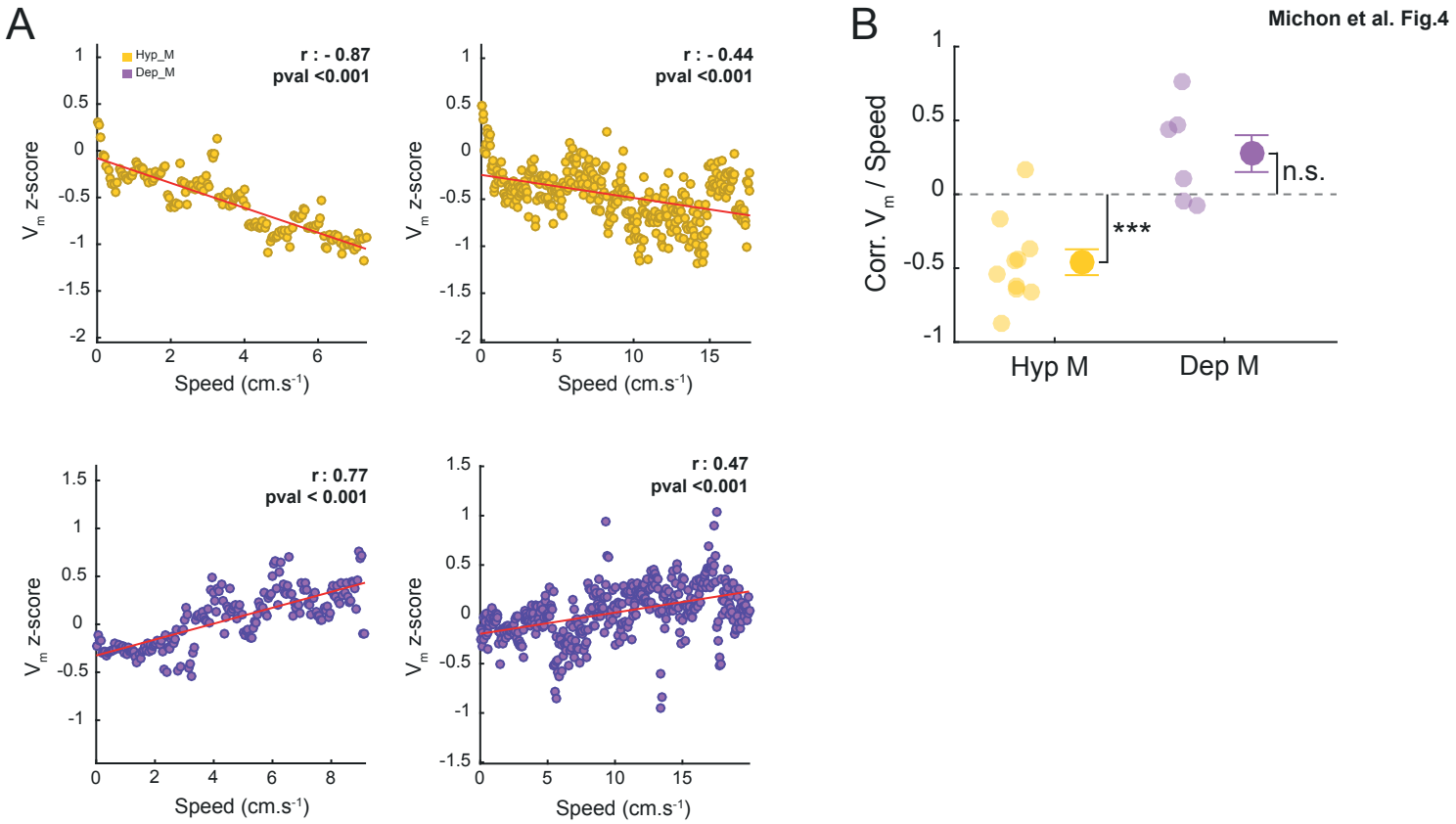


**Fig.4 Speed correlation of Hyp M cells and Dep M cells**

**A.** Example of correlation between speed and subthreshold $V_m$ z-scored in 2 Hyp M cells (up) and 2 Dep M cells (down). Each point corresponds to the mean value of subthreshold $V_m$ z-scored value in speed bins (size of bins: 0.05cm.s-1). **B.** Mean correlation of speed with subthreshold $V_m$ z-scored for Hyp M (r =-0.46 ± 0.09 , n=10, p= $7.54.10^{-4}$, t-test) cells and Dep M cells (r =0.27 ± 0.14 , n=6, p= 0.1, t-test).

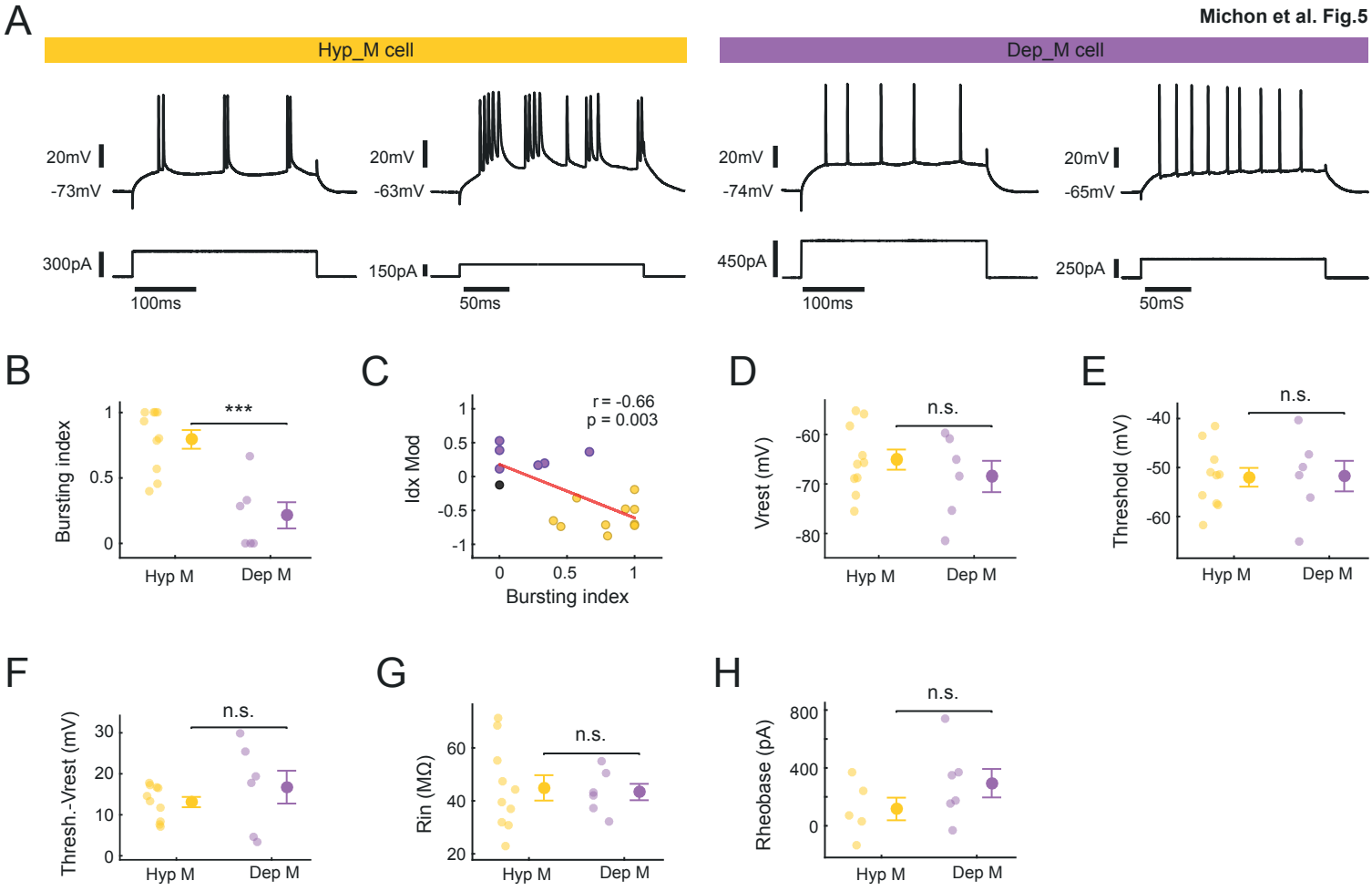


**Fig.5 Intrinsic properties of Hyp M cells vs Dep M cells**

**A.** Firing pattern of two Hyp M and two Dep M cells in response to depolarizing current injection. **B.** Bursting index of Hyp M versus Dep M cells ($mean_{Hyp\ M}$= 0.79 ± 0.08 , n=10, $mean_{Dep\ M}$= 0.21 ± 0.11 , n=6, p= $4.95.10^{-4}$, t-test). **C.** Correlation of the bursting index with index (r=-0.66, p=0.003). **D.** Vrest of Hyp M versus Dep M cells ($mean_{Hyp\ M}$= -65.09 ± 2.15 mV , n=10, $mean_{Dep\ M}$= -68.49 ± 3.47 mV , n=6, p= 0.39, t-test). **E.** Threshold of Hyp_M versus Dep M cells ($mean_{Hyp\ M}$= -51.99 ± 2.02 mV , n=10, $mean_{Dep\ M}$= -51.74 ± 3.42 mV , n=6, p=0.95, t-test). **F.** Thresh-Vrest of Hyp_M versus Dep M cells ($mean_{Hyp\ M}$= 13.10 ± 1.32 mV , n=10, $mean_{Dep}$= 16.74 ± 4.39 mV , n=6 , p=0.36 ,t-test). **G.** Input resistance of Hyp_M versus Dep M cells ($mean_{Hyp\ M}$= 44.9 ± 5.06 MΩ , n=10, $mean_{Dep\ M}$ = 43.3 ± 3.39 MΩ , n=6, p=0.83 ,t-test).H. Rheobase of Hyp M versus Dep M cells ($mean_{Hyp\ M}$= 116.19 ± 87.37 pA , n=5, $mean_{Dep\ M}$ = 294.33 ± 107.81 pA , n=6 , p=0.24 ,t-test).

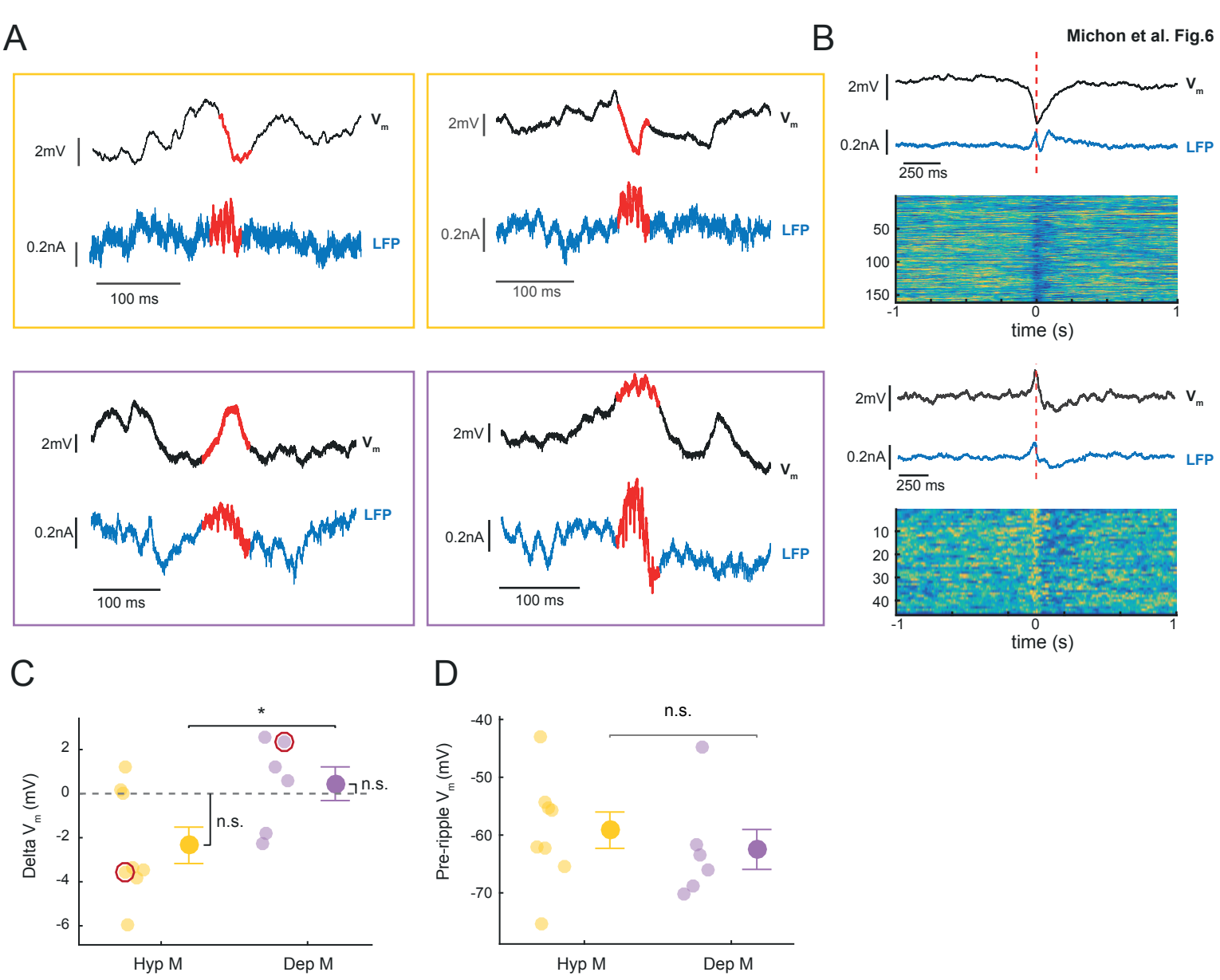


**Fig.6 - Vm modulation of Hyp M cells and Dep M cells during ripples**

**A.** Examples of subth.$V_m$ modulation (black trace) during a ripple (red trace) detected in LFP (blue trace). Up: subthreshold $V_m$ is hyperpolarized during ripple in two Hyp M cell (yellow frame). Down: subthreshold $V_m$ is depolarized during ripple in two Dep M cell (purple frame). **B.** Mean subthreshold $V_m$, associated mean LFP and subthreshold $V_m$ normalized aligned on ripple occurence. Up: example of cell hyperpolarized during ripple. Down: Example of a cell depolarized during ripple. **C.** Mean delta subthreshold $V_m$ modulation during ripple for Hyp M cells ($mean_{Hyp\ M}$= -2.35 ± 0.88 mV, n=8, p= 0.45, ranksum) versus Dep M cells ($mean_{Dep\ M}$= 0.45 ± 0.84 mV, n=6, p= 0.61,t-test) ,(Hyp M vs Dep M, p=0.046, t-test). red circle on Hyp M and Dep M value correspond to mean delta of cell presented respectively in B. **D.** Mean pre-ripple $V_m$ for Hyp M cells versus Dep_M cells ($mean_{Hyp\ M}$= -59.15 ±3.36 mV,n=8 , $mean_{Dep\ M}$= -62.49 ± 3.78 mV, n=6, p=0.52, t-test)

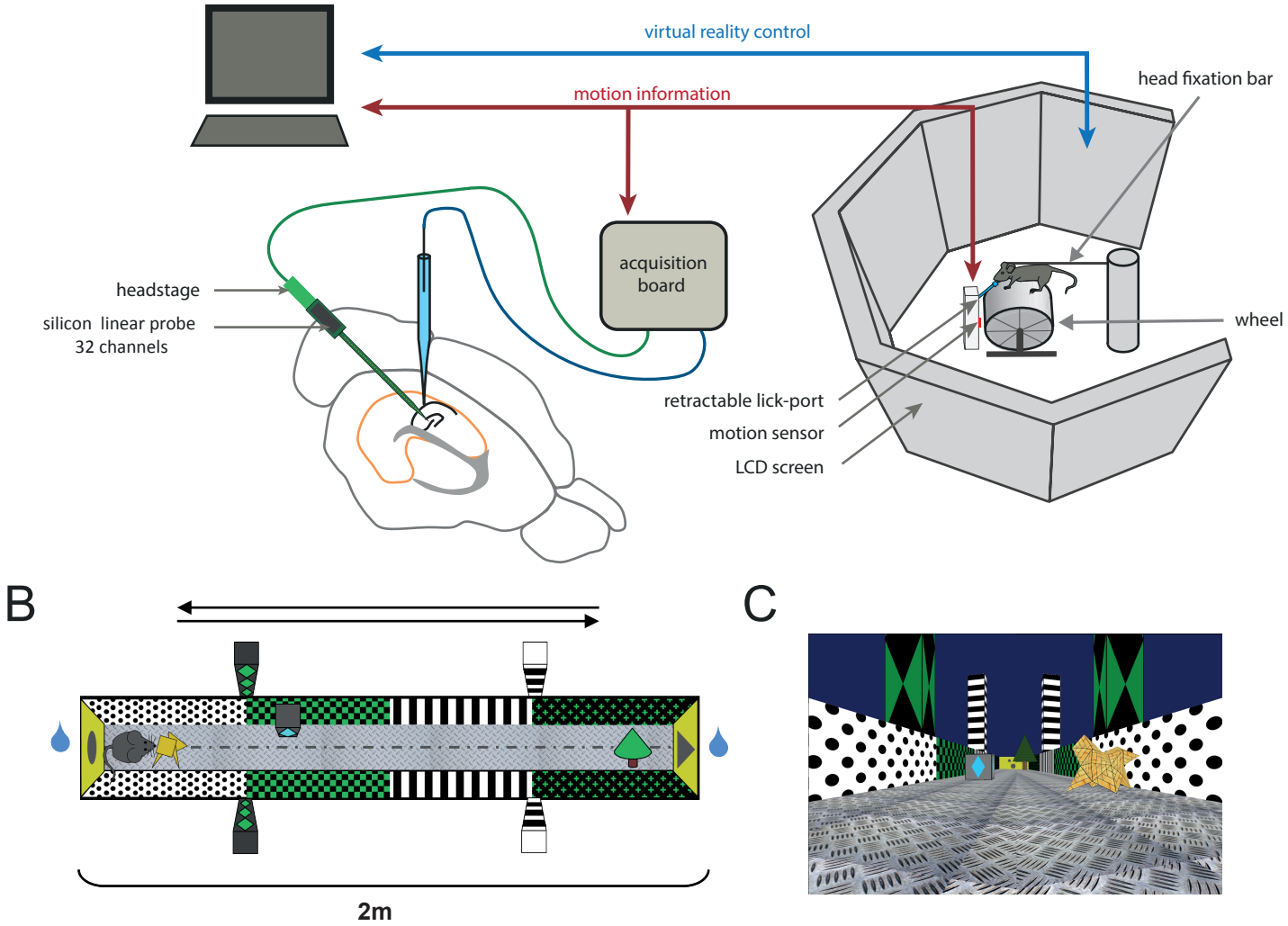


**Article - Figure sup. 1 - Virtual reality setup**

**A.** Schema of the virtual reality set up. The mouse is head-fixed and located on a wheel surrounded by LCD screens where a virtual environment is displayed.
**B.** Schema of the top of view of the linear track.
**C.** first person view of the linear track used

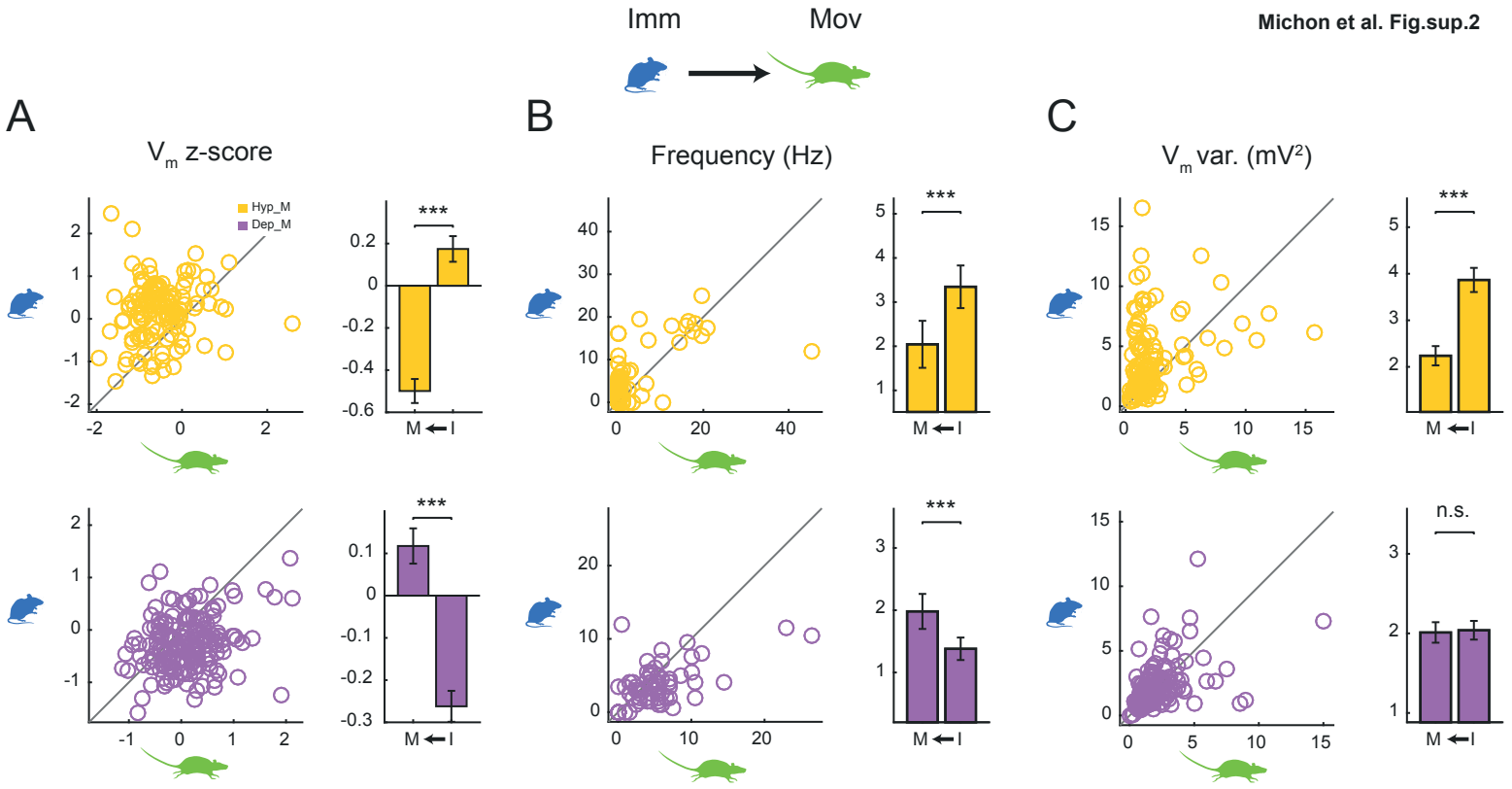


**Article - Figure sup. 8 - Vm modulation of Hyp M cells and Dep M cells during initiation or stop of movement**

**A.** Scatterplots and barplots of Subthreshold $V_m$ z-scored before initiation of movement (immobility ) and after the transition (movement ) for all transitions of Hyp M cells (up) ($\Delta$ = -0.67 ± 0.08, n=127, p=4.82.$10^{-14}$, paired t-test) and Dep M cells (down) cells ($\Delta$ = 0.38 ± 0.05, n=180, p=4.95.$10^{-13}$, paired t-test) **B.** Scatterplots and barplots of Frequency before initiation of movement (immobility ) and after the transition (movement ) for all transitions of Hyp M cells (up) ($\Delta$ = -1.30 ± 0.41 Hz, n=127, p=7.79.$10^{-7}$, signed rank test) and Dep M cells (down) ($\Delta$ = 0.60 ± 0.018 Hz, n=180, p=5.68.$10^{-5}$, signed rank test) **C.** Scatterplots and barplots of Subthresold $V_m$ variance before initiation of movement (immobility ) and after the transition (movement ) for all transitions of Hyp M cells (up)($\Delta$ = -1.63 ± 0.29 $mV^2$, n=127, p=2.96.$10^{-9}$, signed rank test) and Dep M cells (down)($\Delta$ = -0.03 ± 0.13 $mV^2$, n=180, p= 0.359, signed rank test)

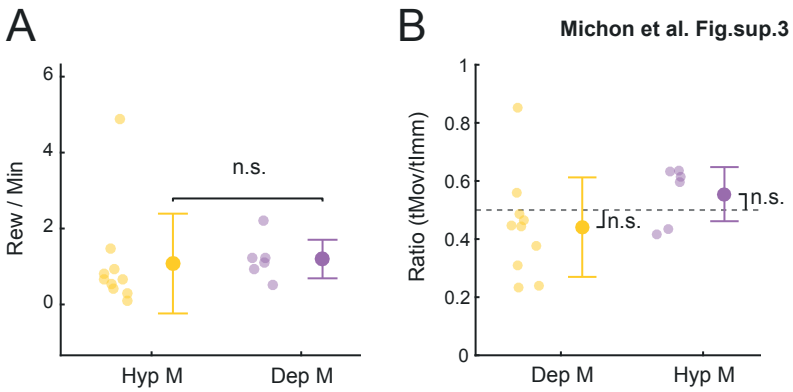


**Article - Figure sup. 0 – Behavior control**

**A.** Mean number of reward per minute for Hyp M cells versus Dep M cells ( $mean_{Hyp\ M}$= 1.08 ± 0.44, n=10, $mean_{Dep\ M}$= 1.2 ± 0.23, n=6, p= 0.18, ranksum test). **B.** Ratio of the time spent in movement on time spent in immobility for Hyp M cells ($mean_{Hyp\ M}$= 0.44 +- 0.06, n=10, p=0.33, t-test) versus Dep M cells ($mean_{Dep\ M}$ = 0.55+-0.04, n=6, p=0.25, t-test ).

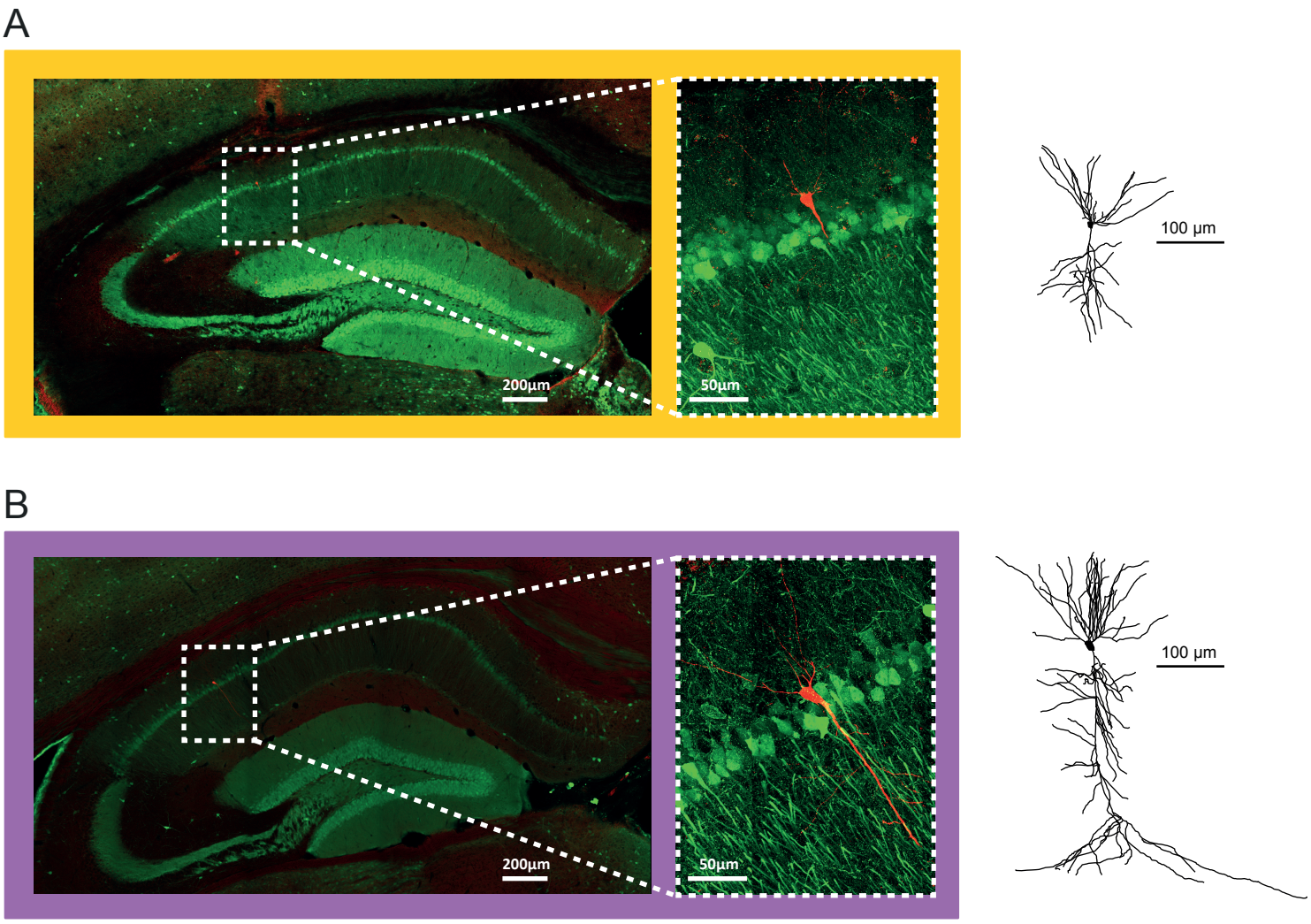


**Figure sup.4 Histology**

**A.** Left : Location and magnification of the revelation of a Hyp M recorded neuron filled with biocytin (red) and labelingof calbindin positiv neurons (green). Right : reconstruction of the same neuron and location on radial axes of CA1 based on calbindin labeling **B.** same as A. but for a Dep M neuron